Monthly Notices
of the
ROYAL ASTRONOMICAL SOCIETY

MNRAS **453,** 1727–1739 (2015) doi:10.1093/mnras/stv1694

Feeding versus feedback in AGN from near-infrared IFU observations XI: NGC 2110

Marlon R. Diniz,[1]★ Rogemar A. Riffel,[1] Thaisa Storchi-Bergmann[2] and Claudia Winge[3]

[1]*Departamento de Física, Centro de Ciências Naturais e Exatas, Universidade Federal de Santa Maria, 97105-900 Santa Maria, RS, Brazil*
[2]*Instituto de Física, Universidade Federal do Rio Grande do Sul, CP 15051, Porto Alegre 91501-970, RS, Brazil*
[3]*Gemini Observatory, c/o AURA, Inc., Casilla 603, La Serena, Chile*

Accepted 2015 July 24. Received 2015 July 23; in original form 2014 September 24

ABSTRACT

We present a two-dimensional mapping of the gas flux distributions, as well as of the gas and stellar kinematics in the inner 220 pc of the Seyfert galaxy NGC 2110, using *K*-band integral field spectroscopy obtained with the Gemini Near-infrared Integral Field Spectrograph at a spatial resolution of ≈24 pc and spectral resolution of ≈40 km s^{-1}. The H_2 λ2.1218 μm emission extends over the whole field of view and is attributed to heating by X-rays from the AGN and/or by shocks, while the Brγ emission is restricted to a bipolar region extending along the south-east–north-west direction. The masses of the warm molecular gas and of the ionized gas are $M_{H_2} \approx 1.4 \times 10^3\,M_\odot$ and $M_{H\,II} \approx 1.8 \times 10^6\,M_\odot$, respectively. The stellar kinematics present velocity dispersions reaching 250 km s^{-1} and a rotation pattern reaching an amplitude of 200 km s^{-1}. The gas velocity fields present a similar rotation pattern but also additional components that we attribute to inflows and outflows most clearly observed in the molecular gas emission. The inflows are observed beyond the inner 70 pc and are associated with a spiral arm seen in blueshift to the north-east and another in redshift to the south-west. We have estimated a mass inflow rate in warm molecular gas of $\approx 4.6 \times 10^{-4}\,M_\odot\,yr^{-1}$. Within the inner 70 pc, another kinematic component is observed in the H_2 emission that can be interpreted as due to a bipolar nuclear outflow oriented along the east–west direction, with a mass outflow rate of $\approx 4.3 \times 10^{-4}\,M_\odot\,yr^{-1}$ in warm H_2.

Key words: galaxies: individual: NGC 2110 – galaxies: ISM – galaxies: kinematics and dynamics – galaxies: Seyfert – infrared: galaxies.

1 INTRODUCTION

A necessary condition for the onset of nuclear activity in galaxies is the presence of gas to feed the nuclear supermassive black hole (hereafter SMBH; Heckman & Best 2014). Evidence for the presence of large quantities of gas in the inner few hundred parsecs of nearby active galaxies has been indeed found in a number of imaging studies (e.g. Malkan, Gorjian & Tam 1998). These studies reveal the presence of dusty structures, in the form of compact nuclear discs, filaments and spirals. In Simões et al. (2007), it was found that, in the particular case of an early-type sample of active and non-active galaxies, all the active galaxies had dusty structures in the inner few hundred parsecs, while only 25 per cent of the non-actives had such structures, implying that the dust was a tracer of the gas feeding the active nucleus. The excess of dust in the active galaxies relative to the non-active ones was later confirmed by a study using *Spitzer* observations to calculate the dust mass of these regions (Martini, Dicken & Storchi-Bergmann 2013). As the inferred gas mass around the active galactic nuclei (AGNs) is much larger than necessary to feed the SMBH inside, these structures are reservoirs of material where new star formation may be triggered.

This connection between the presence of dusty spirals and nuclear activity in galaxies suggests that the gas might be streaming along these structures towards the central region to feed the SMBH inside (Ferrarese & Ford 2005; Somerville et al. 2008; Kormendy & Ho 2013). The dust mass at kpc scales in AGNs is estimated to be in the range 10^5–$10^7\,M_\odot$ (Simões et al. 2007; Martini et al. 2013), and the associated large amounts of molecular gas (10^7 to $10^9\,M_\odot$) reinforce the importance of searching for signatures of molecular gas inflows within the inner kiloparsec.

On the other hand, recent studies have also found massive outflows of molecular gas (Sakamoto et al. 2010; Aalto et al. 2012; Veilleux et al. 2013), in particular, in luminous infrared galaxies and ultra-luminous infrared galaxies.

★E-mail: diniz.mr@gmail.com

Observations of nearby active galaxies using spatially resolved integral field spectroscopy (IFS) provide constraints for the feeding and feedback processes. The study of these processes in nearby AGNs has been carried out using IFS at near-IR bands, which contain emission lines from molecular (tracer of the AGN feeding) and ionized (tracer of the AGN feedback) gas. Most of the observations are performed with adaptive optics using 8–10 m telescopes at spatial resolutions ranging from a few parsecs to tens of parsecs. The main results of these studies are as follows. (i) In general, the molecular and ionized gas present distinct flux distributions and kinematics. The H_2 emission is dominated by rotational motion and shows lower velocity dispersion values than the ionized gas. From the gas excitation and kinematics, we have found that the emitting H_2 gas (hot molecular gas, as it originates in gas at $\approx$2000 K; Storchi-Bergmann et al. 2009) is located in the plane of the galaxy, presenting a velocity field dominated by rotation. In some cases, in the inner $\approx$ 30 pc of the galaxy, compact molecular discs (Riffel & Storchi-Bergmann 2011a; Hicks et al. 2013; Mazzalay et al. 2014; Schönell et al. 2014) and gas inflows along nuclear spirals (e.g. Riffel et al. 2008; Riffel, Storchi-Bergmann & Winge 2013b) are found. The inflow rates in cold molecular gas range from a few tenths to a few solar masses per year (Riffel et al. 2008, 2009, 2013b; Davies et al. 2009; Sánchez et al. 2009; Riffel & Storchi-Bergmann 2011a). (ii) Although the ionized gas kinematics frequently presents a rotating disc component similar to that seen in H_2 for most galaxies, it shows a large contribution from an outflowing component for some objects (Riffel et al. 2006, 2009, 2013b; Storchi-Bergmann et al. 2010; Riffel & Storchi-Bergmann 2011a,b; Barbosa et al. 2014; Riffel, Storchi-Bergmann & Riffel 2014; Schönell et al. 2014). These outflows are most easily seen in the [Fe II] 1.257 and 1.644 μm emission lines, present in the near-IR spectra. In Barbosa et al. (2014), it is shown that these lines seem to be better tracers of AGN outflows than the previously used [O III] λ5007 Å emission line. This is due to the fact that the [Fe II] emission is more extended than that of the [O III], reaching out to the partially ionized region (beyond the fully ionized region). Mass outflow rates in ionized gas have been estimated to be in the range from 0.05 to 6 $M_\odot$ yr^{-1} (Storchi-Bergmann et al. 2010; Riffel & Storchi-Bergmann 2011b; Riffel et al. 2013b; Barbosa et al. 2014).

In this work, we present adaptive optics-assisted *K*-band IFS of the inner 3 arcsec × 3 arcsec of the galaxy NGC 2110 obtained with Gemini NIFS. The results shown here are part of a larger project of the AGNIFS (AGN Integral Field Spectroscopy) group to map inflows and outflows in a complete sample of AGN, selected by their X-ray emission. NGC 2110 is an early-type S0 galaxy which hosts a Seyfert 2 nucleus, located at a distance of 30.2 Mpc, assuming a redshift $z = 0.007\,789$ (NED[1]), where 1 arcsec corresponds to 146 pc at the galaxy. Due to its proximity, it has been already observed in several wavebands, from radio to X-rays. NGC 2110 is one of the brightest nearby Seyfert galaxies in hard X-rays (2–10 keV) and is classified as a narrow-line X-ray galaxy (Bradt et al. 1978). Its luminosity is comparable to that observed for Seyfert 1 nuclei and soft X-ray emission was observed extending up to 4 arcsec to the north of the nucleus (Weaver et al. 1995). Dust lanes and asymmetries are seen up to 4 arcsec west of the nucleus in optical (Malkan et al. 1998) and near-IR (Quillen et al 1999) broad-band images obtained with the *Hubble Space Telescope* (*HST*). Storchi-Bergmann et al. (1999) obtained long-slit near-IR spectroscopy of the inner ∼10 arcsec of NGC 2110 along the major and minor axes of NGC 2110 finding strong emission of both [Fe II] and H_2, as well as signatures of distinct kinematics for these two species. Excitation by X-rays was favoured for H_2, while shocks were concluded to be also important for excitation of the [Fe II].

Observations in radio reveal extended emission in an S-shaped structure, with an extent of ≈4 arcsec along the north–south direction (Ulvestad & Wilson 1983; Nagar et al. 1999). Circumnuclear extended gas emission was studied by Evans et al. (2006) using *Chandra*, *HST* and Very Large Array (VLA) observations. Long-slit spectroscopic observations of the inner 10 arcsec (González Delgado et al. 2002; Ferruit et al. 2004) have shown that the gas velocity field is asymmetric relative to the nucleus at distances larger than 1 arcsec, while within the inner 1 arcsec a blueshift excess is observed, suggesting the presence of a nuclear outflow. Rosario et al. (2010) have shown that the outflow is oriented at a position angle (PA) offset by ≈40° from the PA of the radio jet and suggested that the gas is ionized by the central AGN and not by shocks.

The gas kinematics was first investigated by Wilson & Baldwin (1985) and Wilson, Baldwin & Ulvestad (1985), who reported a rotation pattern in the ionized gas kinematics, similar to those observed for other spiral galaxies, suggesting that the gas is in rotation in the galaxy disc. They found that the rotation centre was located 1.7 arcsec south of the photometric nucleus and observed asymmetric profiles in the [O III] to the south-east. In the long-slit near-IR spectroscopic observations of Storchi-Bergmann et al. (1999), they also found a displacement of the kinematic nucleus, but smaller than the optical, thus attributed at least partially to obscuration, which is smaller in the near-IR than in the optical. Recent optical IFS with the Gemini Multi-Object Spectrographs (GMOS) by Schnorr-Müller et al. (2014) revealed the presence of four distinct kinematic components in the emitting gas: a cold gas disc, a warm gas disc, a compact nuclear outflow and a high-latitude cloud identified as 'the northern cloud'. They also observed excess blueshifts and redshifts in the cold gas disc kinematics relative to rotational motion that were attributed to inflows and outflows. They have shown that the apparent asymmetry of the gas velocity field is due to the superposition of the contribution of the different components; when this is taken into account, there is no more asymmetry in the velocity fields.

Studies of the nuclear stellar population by González Delgado, Heckman & Leitherer (2001) using optical continuum images did not show signatures of a young stellar population (age ≤ 1 Gyr). On the other hand, Durré & Mould (2014) used near-IR (*Z*, *J* and *H* bands) IFS of the inner 0.8 arcsec obtained with the OSIRIS instrument at the Keck Telescope at an angular resolution of 70 mas, and reported the detection of four star-forming clusters at distances smaller than 0.3 arcsec from the galaxy nucleus. They also found that the ionized gas (in particular [Fe II]) surrounding the star clusters is being excited by strong outflows associated with recent star formation and derived star formation rates of 0.12–0.26 $M_\odot$ yr^{-1}. The new findings by Durré & Mould (2014) and Schnorr-Müller et al. (2014), relative to previous studies, can be attributed to the better spatial coverage of IFS to study the central region of galaxies when compared to long-slit studies. Durré & Mould (2014) also calculated the SMBH mass using the He I velocity profile considering a simple Keplerian rotation in a region with radius 56 pc and found a mass for the SMBH of $\approx 4 \times 10^8$ $M_\odot$. Using the M–σ relationship, they find a value of $\approx 3 \times 10^8$ $M_\odot$, while with the Graham et al. (2011) updated relationship for elliptical galaxies they derive a value of $\approx 5 \times 10^7$ $M_\odot$; a lower value for the SMBH mass was also obtained using the [Fe II] velocity field, probably due to the presence of outflows from the clusters.

[1] NASA/IPAC Extragalactic Database.

This paper is organized as follows. In Section 2 we describe the observations and data reduction procedures. The results are presented in Section 3 and discussed in Section 4. We present our conclusions in Section 5.

2 OBSERVATIONS AND DATA REDUCTION

The near-IR observations of NGC 2110 were obtained with the integral field spectrograph NIFS (McGregor et al. 2003) on the Gemini North telescope in two distinct nights, under the programme GN-2010B-Q-25. In the first night, five exposures of 600 s were obtained for the galaxy, three observations with the same exposure time for the sky and three exposures of 18 s each for the telluric star. In the second night, only one exposure of 600 s for the galaxy and for the sky and four observations of 15 s for the telluric standard star were obtained.

The data reduction was performed using specific tasks contained in the NIFS package which is part of GEMINI IRAF package. The reduction process followed standard procedures such as trimming of images, flat-fielding, sky subtraction, wavelength and spatial distortion calibrations. The telluric absorptions were removed using the spectrum of the telluric standard star, and the flux calibration was performed by interpolation a blackbody function to the spectrum of the telluric standard star. We combined the individual data cubes into a single data cube using the *gemcombine* task of the GEMINI IRAF package and used the *sigclip* algorithm to eliminate the remaining cosmic rays and bad pixels, using the peak of the continuum as reference for astrometry for the distinct cubes. The final data cube covers the inner 3 arcsec × 3 arcsec (∼440 × 440 pc^2) region and contains ∼3900 spectra, each spectrum corresponding to an angular coverage of 0.05 arcsec × 0.05 arcsec, which translates into ∼7 × 7 pc^2 at the galaxy.

The spectral resolution of the data is about 3.4 Å at 2.3 μm, measured from the full width at half-maximum (FWHM) of the arc lamp lines and corresponds to a velocity resolution of 44 km s^{-1}. The angular resolution is 0.15 arcsec, corresponding to ≈22 pc at the galaxy, and was obtained from the FWHM of a Gaussian curve fitted to the flux distribution of the standard star. A similar FWHM is found by fitting the unresolved nuclear *K*-band continuum emission, attributed to the emission of the dusty torus.

For illustration purposes, we rebinned each spaxel to 1/3 of its original size (0.05 arcsec) to smooth the flux and kinematics maps. We applied the same procedure to the continuum image of the standard star and noticed that the effect of this procedure on the measured FWHM is smaller than 5 per cent, and thus the rebinning of the maps does not degrade the spatial resolution of the data significantly.

3 RESULTS

The left-hand panel of Fig. 1 shows an optical image of NGC 2110 obtained with the *HST* Wide Field Planetary Camera 2 through the filter *F606W*. The field of view (FOV) of the NIFS observations (3 arcsec × 3 arcsec) is indicated by the grey square. In the right-hand panel, we present a continuum image of the nuclear region obtained from the NIFS data cube by calculating the average of the fluxes between 2.25 to 2.28 μm, a region with no emission lines. In the bottom panel, we present four spectra, extracted within a circular aperture with radius of 0.25 arcsec at the positions marked in the *K* continuum image. The position '+' corresponds to the location of the nucleus, defined as the peak of the continuum emission. The position A [$(x, y) = (-0.2$ arcsec, -0.2 arcsec)] was chosen to represent a typical extranuclear spectrum, the position B [with coordinates $(x, y) = (0.0$ arcsec, 0.7 arcsec) relative to the nucleus] is located 0.7 arcsec north of the nucleus and corresponds to a location where a region of enhanced H_2 line emission is observed (as seen at the top panel of Fig. 3). Position C [$(x, y) = (0.2$ arcsec, 0.4 arcsec)] corresponds to a location of enhanced Brγ emission at 0.4 arcsec north-west of the nucleus. It can be seen that the extranuclear spectra are very similar (positions A, B and C), while the nuclear spectrum (marked with the '+' sign) is much redder, probably due to emission of the dusty torus. At most positions the spectra display several emission lines of H_2, Brγ, as well as the CO absorption band heads around 2.3 μm. These lines are identified in the spectra and have allowed us to obtain the gas and stellar kinematics, as discussed below.

3.1 Stellar kinematics

We have used the penalized pixel-fitting (PPXF) method of Cappellari & Emsellem (2004) to derive the stellar kinematics, by fitting the ^{12}CO λ2.29, ^{12}CO λ2.32 and ^{13}CO λ2.34 μm stellar absorptions in the *K* band following the procedure described in Riffel et al. (2008). The library of 60 stellar templates of early-type stars (Winge, Riffel & Storchi-Bergmann 2009) was used to obtain the stellar line-of-sight velocity distribution at each position.

The top panel of Fig. 2 presents the velocity (V_*) map from which we subtracted the systemic velocity, obtained by fitting the velocity field as discussed in Section 4.1. This map shows a rotation pattern with blueshifts to the north-west and redshifts to the south-east of the nucleus, with a maximum velocity of ≈200 km s^{-1} and a major axis along the north–south direction at PA ≈ 170°. The bottom panel displays the stellar velocity dispersion (σ_*) map with values ranging from 50 to 300 km s^{-1}. White regions in the V_* map and black regions in the σ_* map correspond to positions where the signal-to-noise ratio in the CO bands was not high enough to allow good fits. At the nucleus of the galaxy, we could not obtain good fits due to the dilution of the CO absorptions by non-stellar continuum emission. The dilution may be caused by emission of hot dust, as seen in the nuclear spectrum shown in Fig. 1. The uncertainties were derived from the PPXF routine and are smaller than 30 km s^{-1} for both the V_* and σ_* maps.

3.2 Emission-line flux distributions

In order to construct maps for the gas flux distributions, centroid velocities and velocity dispersions, we fitted the emission lines of H_2 and Brγ with Gaussian curves using a modified version of the emission-line profile fitting routine PROFIT (Riffel 2010). This is an automated routine written in IDL language and can be used to fit emission lines with Gaussian curves or Gauss–Hermite series using the MPFITFUN routine (Markwardt 2009) to perform the non-linear least-squares fit. More details of the routine can be found in Riffel (2010).

The flux distributions for the emission lines H_2 λ2.1218 and Brγ λ2.1661 μm (in units of 10^{-17} erg s^{-1} cm^{-2}) are shown, respectively, in the top and bottom panels of Fig. 3. The H_2 λ2.1218 μm flux map shows emission over the whole FOV, with two regions of higher intensity relative to the surrounding regions, one at the nucleus and other at ≈0.7 arcsec to the north of it. The flux distributions for other seven emission lines of H_2 (H_2 λ2.223 44, H_2 λ2.247 76, H_2 λ2.408 47, H_2 λ2.413 67, H_2 λ2.421 80, H_2 λ2.436 97 and H_2 λ2.454 85 μm) are similar to that of H_2 λ2.1218 μm, presenting

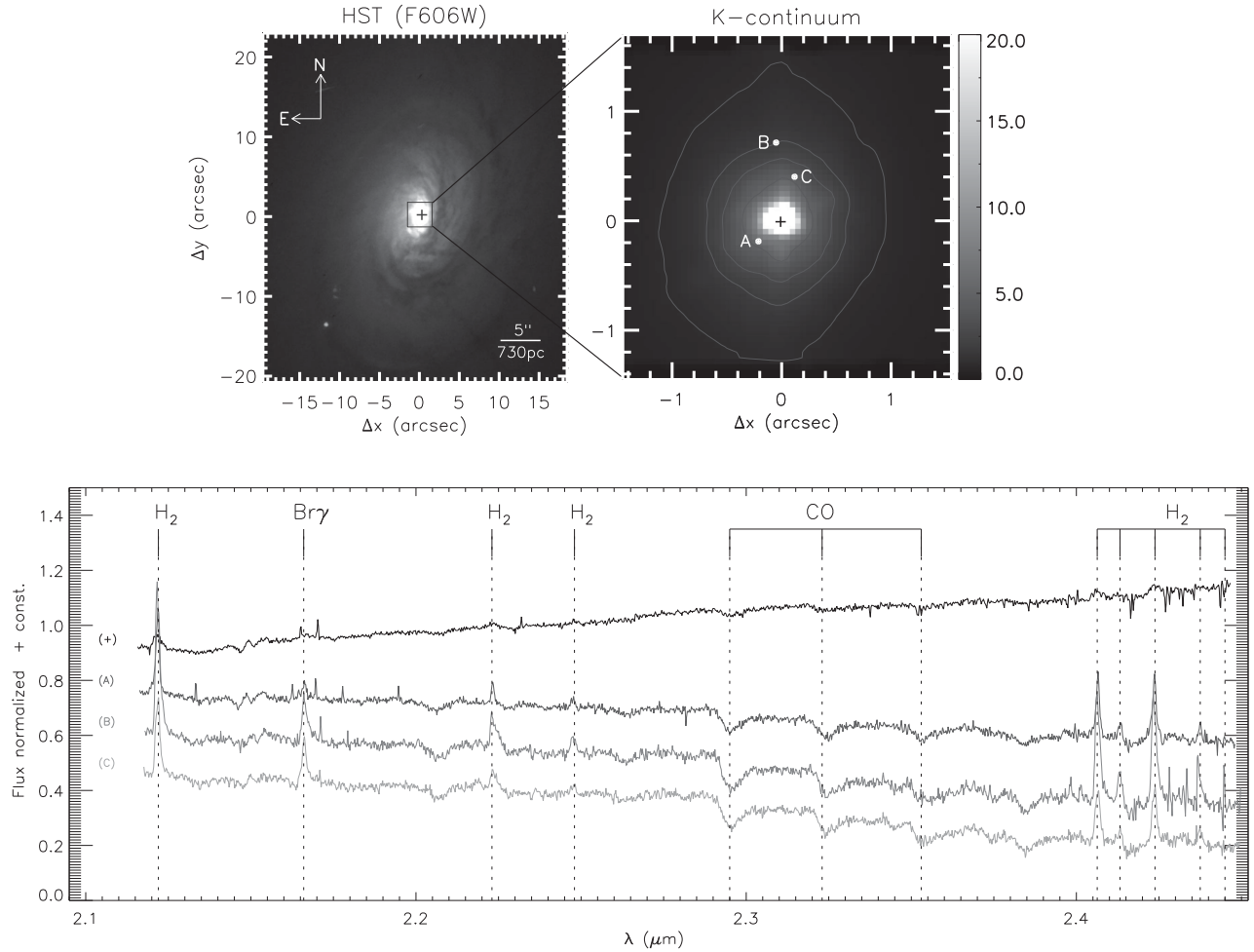

Figure 1. The top-left panel shows an *HST* image of NGC 2110 with the filter *F*606*W*, with the FOV of the NIFS observations indicated by the central square. The top-right panel shows an average continuum image (obtained in the spectral range between 2.25 and 2.28 μm) in flux units of 10^{-17} erg s^{-1} cm^{-2} Å^{-1}; the central cross indicates the position of the nucleus and the other points indicate the positions from which the spectra were extracted. The bottom panel displays the spectra in arbitrary flux units per wavelength, which were extracted within a circular aperture with radius of 0.25 arcsec and corrected for Doppler shift.

however a lower signal-to-noise ratio and for this reason they are not shown.

The Brγ flux map shows emission only covering part of the FOV being extended along the south-east–north-west direction, with the peak flux at ≈0.4 arcsec north-west of the nucleus. The uncertainties in flux are smaller than 20 per cent at most locations for both emission lines, and black regions in Fig. 3 correspond to locations where the uncertainties are larger than 50 per cent and no reliable fits were obtained.

Table 1 displays the fluxes for the detected emission lines at positions A (next to the nucleus), B (the northern blob of enhanced emission in the H_2 flux map of Fig. 3) and C (corresponding to the peak of the Brγ emission at 0.4 arcsec north-west of the nucleus in the flux map of Fig. 3), integrated within a circular aperture of radius 0.25 arcsec.

3.3 Centroid velocity and velocity dispersion maps for the emitting gas

The top panel of Fig. 4 shows the centroid velocity map for the molecular gas in units of km s^{-1}. The systemic velocity, as determined from the fit of the stellar velocity field, was subtracted and the cross indicates the position of the nucleus. The H_2 velocity field shows a rotation pattern with blueshifts to the north (thus approaching) and redshifts to the south (thus receding), with a velocity amplitude of ≈200 km s^{-1}. But, although presenting similar rotation to that observed in the stellar velocity field (Fig. 2), the H_2 velocity field presents additional components. Two structures resembling spiral arms are observed: one to the north in blueshift and the other to the south in redshift. Closer in, excess blueshifts are observed to the west and excess redshifts to the east, at distances from the nucleus smaller than 0.5 arcsec (73 pc). The dark grey curves with an arrow represent the gas flowing to the central region along nuclear spirals.

Fig. 5 shows the velocity dispersion (σ) maps for the H_2 and Brγ emitting gas. Both maps have been corrected for the instrumental broadening. The top panel shows the σ map for the H_2 λ2.1218 μm emission line, with uncertainties of ≈10 km s^{-1}. High velocity dispersions of ≈150 km s^{-1} are seen in a region extending along PA ≈ −45° from north-east to south-west, and lower values of ≈60 km s^{-1} are observed in all other regions.

The Brγ σ map is shown in the bottom panel of Fig. 5, with mean uncertainties of 15 km s^{-1} and presents somewhat higher σ values than those observed for the H_2 in the same regions. At most locations, $\sigma \approx 100$ km s^{-1} are observed in the regions where the H_2 σ is ≈60 km s^{-1}.

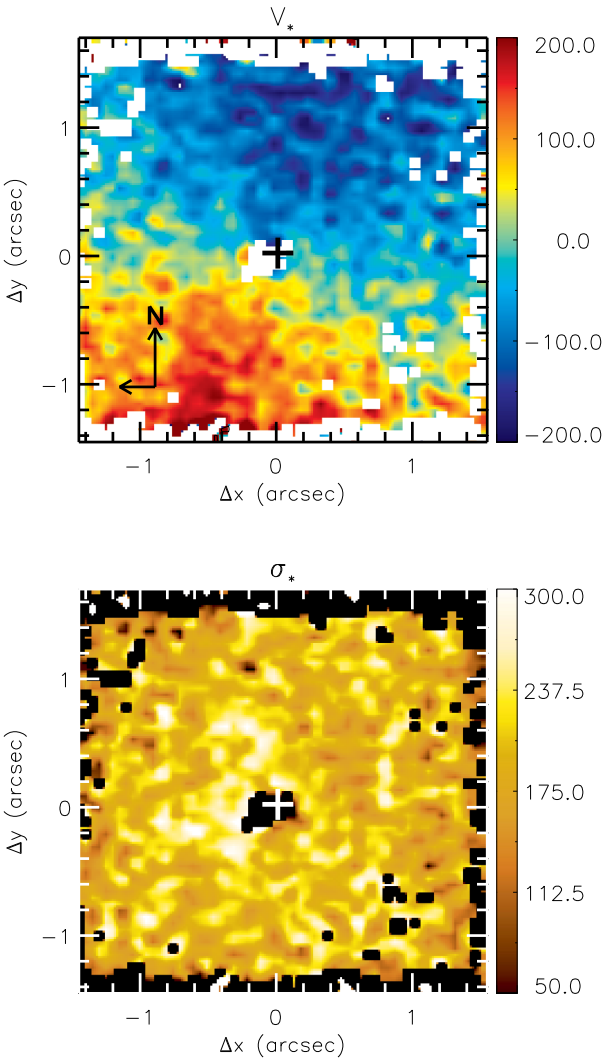

Figure 2. Stellar kinematic maps obtained from the PPXF fit. Top: centroid velocity map. Bottom: velocity dispersion map. The colour bar shows the velocity values in units of km s^{-1} and the central cross marks the position of the nucleus.

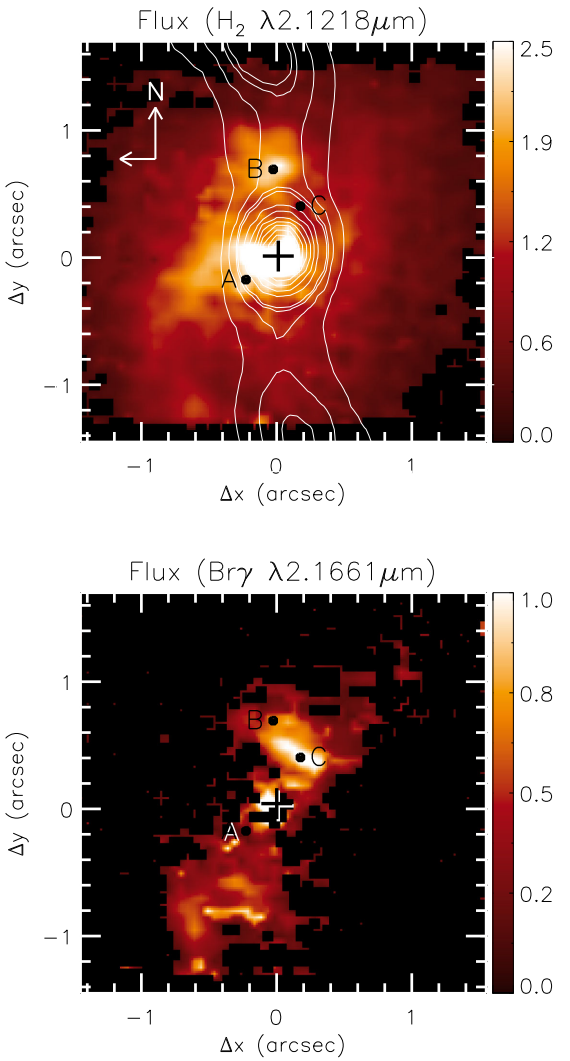

Figure 3. Top: H_2 flux distribution. Bottom: Brγ flux distribution. The central cross marks the position of the nucleus, the colour bars show the range of flux values for each emission line in units of 10^{-17} erg s^{-1} cm^{-2} and white contours correspond to the radio emission.

3.4 Channel maps

Figs 6 and 7 show channel maps along the H_2 λ2.1218 μm and Brγ emission line, respectively. In each panel, the flux distributions have been integrated within velocity bins of 60 km s^{-1}, corresponding to two spectral pixels. The flux distributions are shown in logarithmic units, and the central velocity of each panel (relative to the systemic velocity of the galaxy) is shown in the top-left corner. The central cross marks the position of the nucleus.

Fig. 6 shows that the molecular hydrogen presents emission from gas with velocities in the range from −300 to +350 km s^{-1}. The highest blueshifts are seen at 1 arcsec north of the nucleus, and at a small region surrounding the nucleus, while the highest redshifts are observed predominantly to the south of the nucleus at distances 1 arcsec from it and between the nucleus and 0.2 arcsec to the east. At lower velocities (from ≈−100 to +100 km s^{-1}), the H_2 emission spreads over a larger part of the FOV with the highest intensity structure moving from north-west to south-east as the central velocities change from blueshifts to redshifts.

The channel maps across the Brγ emission-line profile are shown in Fig. 7. The highest blueshifts and redshifts are observed to the north-west and south-east of the nucleus, respectively. There is a trend similar to that observed for H_2 for velocities between ≈ −100 and + 170 km s^{-1}: as the velocities change from blueshifts to redshifts, the highest intensities move from north-west to south-east of the nucleus.

4 DISCUSSION

4.1 Stellar kinematics

González Delgado et al. (2002) presented a study of the stellar kinematics of the central region of NGC 2110 based on optical long-slit observations along PA = 6° of the Ca II triplet (λλ8498, 8542, 8662) absorption lines. They measured a velocity amplitude of ≈180 km s^{-1}, with the line of nodes oriented along PA =163° and velocity dispersion of ≈260 ± 20 km s^{-1}. This σ value agrees, within the uncertainties, with that obtained by Nelson & Whittle (1995) ($\sigma = 220 \pm 25$ km s^{-1}) using Mg*b* lines.

Ferruit et al. (2004) obtained the stellar kinematics from Mg and Fe absorptions lines in the optical with the integral field

Table 1. Emission-line fluxes (units of 10^{-16} erg s^{-1} cm^{-2}) for the A, B and C regions identified in Fig. 3 integrated within a circular aperture with radius of 0.25 arcsec.

λ_0 (μm)	ID	Nuc	A (0.2 arcsec SE)	B (0.7 arcsec N)	C (0.45 arcsec NW)
2.121 83	H_2 1-0S(1)	17.3 ± 4.2	5.55 ± 0.86	5.95 ± 0.93	4.14 ± 0.19
2.166 12	HIBrγ	–	1.12 ± 0.10	1.33 ± 0.19	2.46 ± 0.59
2.223 44	H_2 1-0 S(0)	–	1.14 ± 0.11	2.14 ± 0.41	1.41 ± 0.18
2.247 76	H_2 2-1 S(1)	–	0.83 ± 0.08	0.68 ± 0.05	0.48 ± 0.05
2.408 47	H_2 1-0 Q(1)	–	3.23 ± 0.48	4.52 ± 0.57	3.34 ± 0.26
2.413 67	H_2 1-0 Q(2)	–	0.84 ± 0.10	1.54 ± 0.57	0.90 ± 0.33
2.421 80	H_2 1-0 Q(3)	–	4.24 ± 0.36	4.45 ± 0.48	3.38 ± 0.20
2.436 97	H_2 1-0 Q(4)	–	0.79 ± 0.07	1.34 ± 0.18	0.67 ± 0.18
2.454 85	H_2 1-0 Q(5)	–	2.86 ± 0.26	5.04 ± 0.50	1.93 ± 0.77

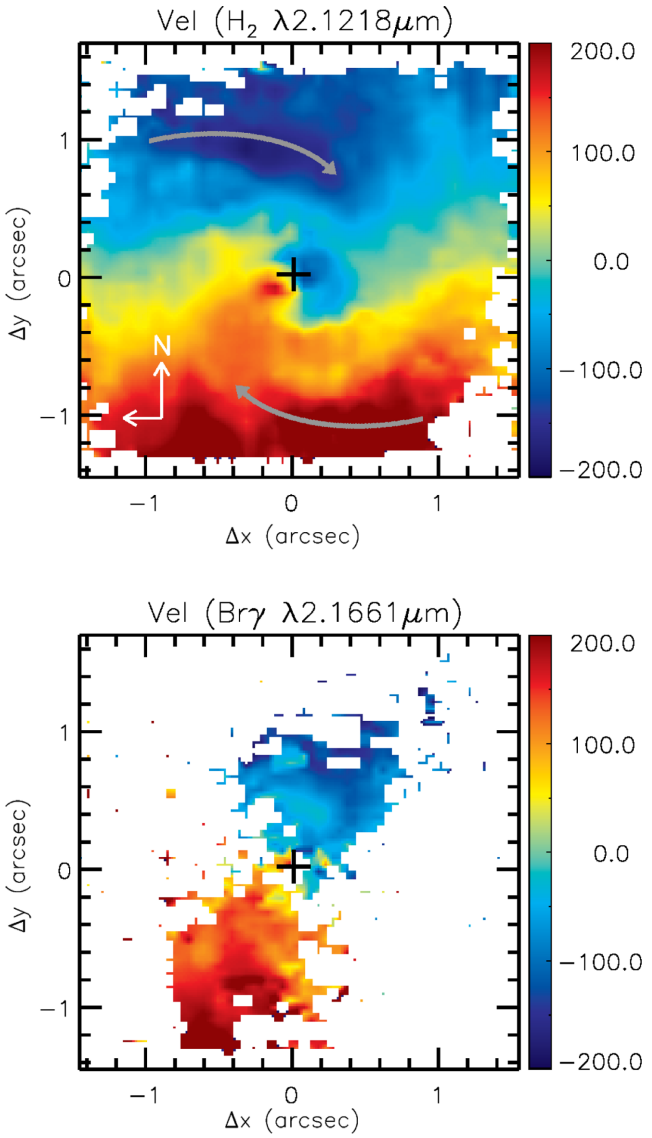

Figure 4. Top panel: velocity field of the H_2 emitting gas. Bottom panel: velocity field of the Brγ emitting gas, restricted around PA ≈ −30°/150°. The colour bars are in units of km s^{-1} and the mean uncertainty in velocity is less than 10 km s^{-1}. The spirals delineated by the grey curves shown in the H_2 velocity map mark the location of the inferred inflows discussed in Section 4.4.1. In both maps, regions with errors higher than 50 per cent in flux were masked out, as for the flux map.

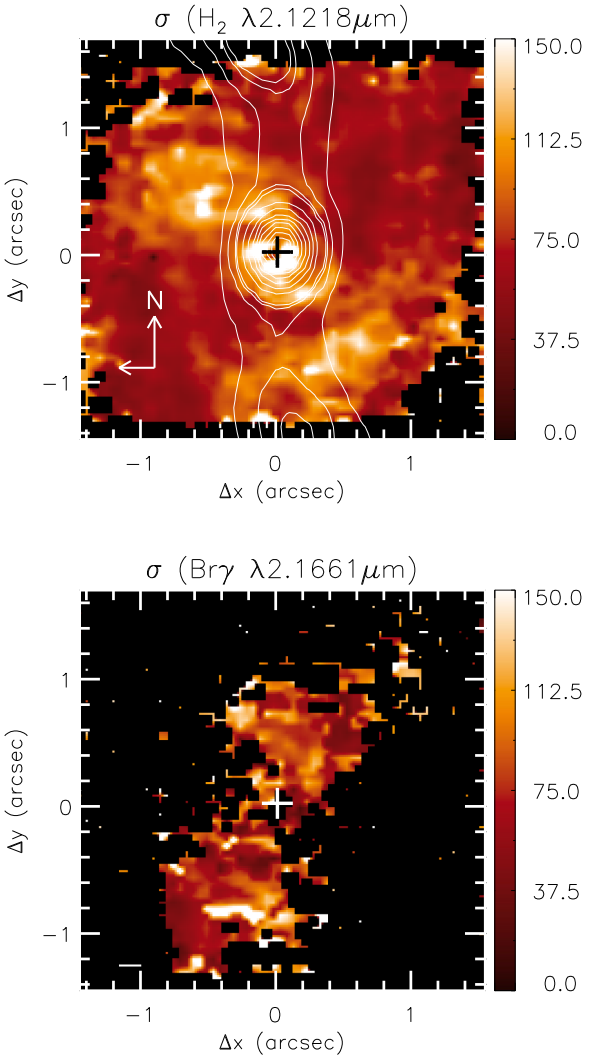

Figure 5. Top: velocity dispersion map for H_2 with contours of the 3.6 cm VLA radio map superimposed. Bottom: velocity dispersion map for Brγ. Both maps are in units of km s^{-1}.

spectrograph OASIS of the Canada–France–Hawaii Telescope in the spectral range 4760–5560 Å over a 4 arcsec × 4 arcsec FOV. They found a velocity amplitude of ≈200 km s^{-1} with the orientation of the line of nodes being consistent with the orientation of the photometric major axis of the galaxy – PA = 163°. The authors also fitted the near-IR CO absorption band heads from long-slit spectroscopy

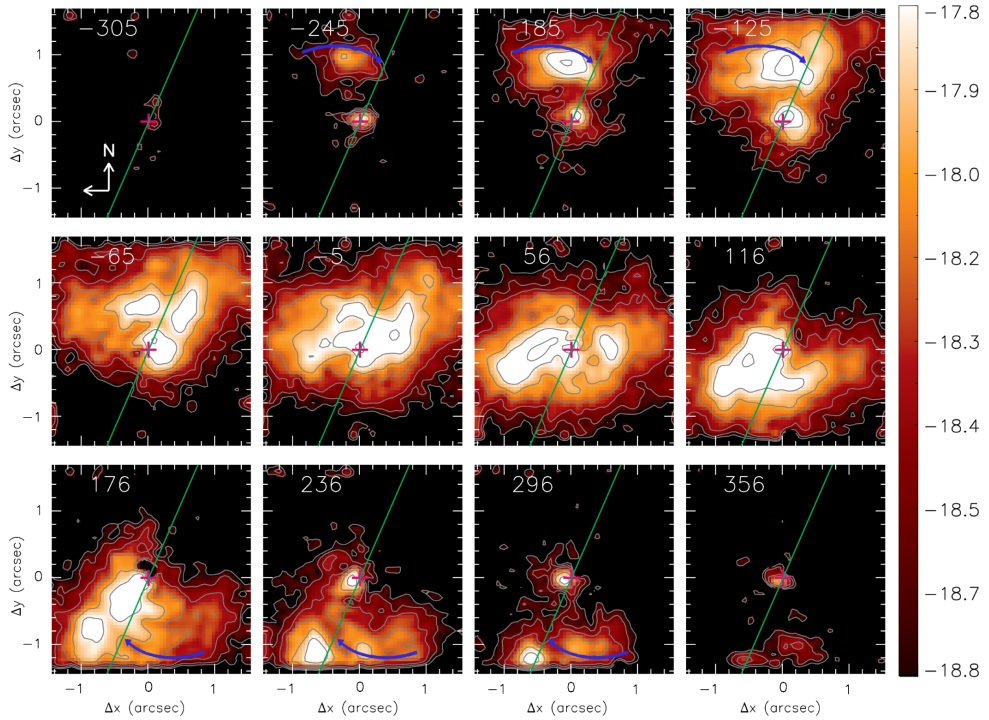

Figure 6. Velocity channels along the H_2 emission line in ≈60 km s^{-1} bins (larger than velocity resolution of the data FWHM ≈44 km s^{-1}) centred on the velocities indicated in each panel. The central cross marks the position of the nucleus (peak of continuum emission), the intensities are represented in the colour scale to the right in logarithmic units and the green line corresponds to the line of nodes. The spiral arms are delineated by the blue curves shown in the H_2 channel maps indicating the location of the inferred inflows discussed in Section 4.4.1.

obtained with the NIRSPEC instrument of the Keck-II Telescope. They found a good correspondence between the NIRSPEC and OASIS measurements.

In order to compare our stellar velocity field with those obtained in the previous studies described above, we have fitted a rotating disc model to the stellar velocity field of Fig. 2, assuming circular orbits in the plane of the galaxy, as in Bertola et al. (1991):

$$V(R,\Psi) = V_s + \frac{A R \cos(\Psi-\Psi_0)\sin(i)\cos^p\theta}{R^2[\sin^2(\Psi-\Psi_0)+\cos^2(i)\cos^2(\Psi-\Psi_0)]+c_0^2\cos^2(i)^{p/2}}, \quad (1)$$

where R and Ψ are the coordinates of each pixel in the plane of the sky, V_s is the systemic velocity, A is the amplitude of the rotation curve at the plane of the galaxy, Ψ_0 is the position angle of the line of nodes, c_0 is a concentration parameter, i is the disc inclination relative to the plane of the sky and p is a model fitting parameter. For $p = 3/2$ the system has a finite mass, as for a Plummer potential (Plummer 1911), and for $p = 1$ the rotation curve is asymptotically flat.

The top-panel of Fig. 8 shows the rotating disc model that provided the best fit of the observed velocities. In the bottom panel, we show the residual map, obtained from the subtraction of the model from the observed velocities. Although at some locations the residuals are larger than the calculated uncertainties, the residual map does not show any systematic structure, and presents residuals larger than 50 km s^{-1} only for 13 per cent of the spaxels. We thus conclude that the model is a good representation of the stellar velocity field. The parameters derived from the fit are systemic velocity corrected to the heliocentric reference frame $V_s = 2332 \pm 15$ km s^{-1}, $\Psi_0 = 162^\circ \pm 0.^\circ6$, $A = 306 \pm 10.5$ km s^{-1}, $i = 43^\circ \pm 2.^\circ5$ and $c_0 = 0.9 \pm 0.04$ arcsec. The location of the kinematical centre was fixed at $X_0 = Y_0 = 0$ arcsec and p was limited to range between 1 and 1.5, which is the range of values expected for galaxies (Bertola et al. 1991). The best fit was obtained with $p = 1.5$. The systemic velocity and the inclination of the disc are in good agreement with those listed in the NED data base. The orientation of the line of nodes agrees with the one quoted in González Delgado et al. (2002).

We can also compare our results with those obtained for the gas kinematics by Schnorr-Müller et al. (2014) using the GMOS Integral Field Unit (IFU) for the inner 1.1 × 1.6 kpc^2 of NGC 2110. They identified four components in the emitting gas named as (1) warm gas disc ($\sigma = 100$–220 km s^{-1}), (2) cold gas disc ($\sigma = 60$–90 km s^{-1}), (3) nuclear component ($\sigma = 220$–600 km s^{-1}) and (4) northern cloud ($\sigma = 60$–80 km s^{-1}). They fitted the velocity field of the disc components by a rotation model similar to the one used here. For the cold component, they found $V_s = 2309 \pm 10$ km s^{-1}, $\Psi_0 = 171^\circ \pm 1^\circ$ and $i = 39^\circ \pm 1^\circ$. For the warm component, they found $V_s = 2308 \pm 11$ km s^{-1}, $\Psi_0 = 169^\circ \pm 1^\circ$, keeping the inclination fixed to the same value of the cold disc. The parameters for both disc components are similar to those we obtained for the stellar kinematics, as well as the amplitude of the velocity field in the inner 1.5 arcsec obtained for the optical emitting gas.

The average stellar velocity dispersion obtained from the measurements shown in Fig. 2 is $\sigma_\star = 200 \pm 20$ km s^{-1}, which is somewhat smaller than those obtained by González Delgado et al. (2002) and Nelson & Whittle (1995) using optical absorption lines as mentioned above. However, Riffel et al. (2015a) showed that the σ_* obtained using CO band heads is systematically smaller than the values obtained from the fitting of optical absorption lines

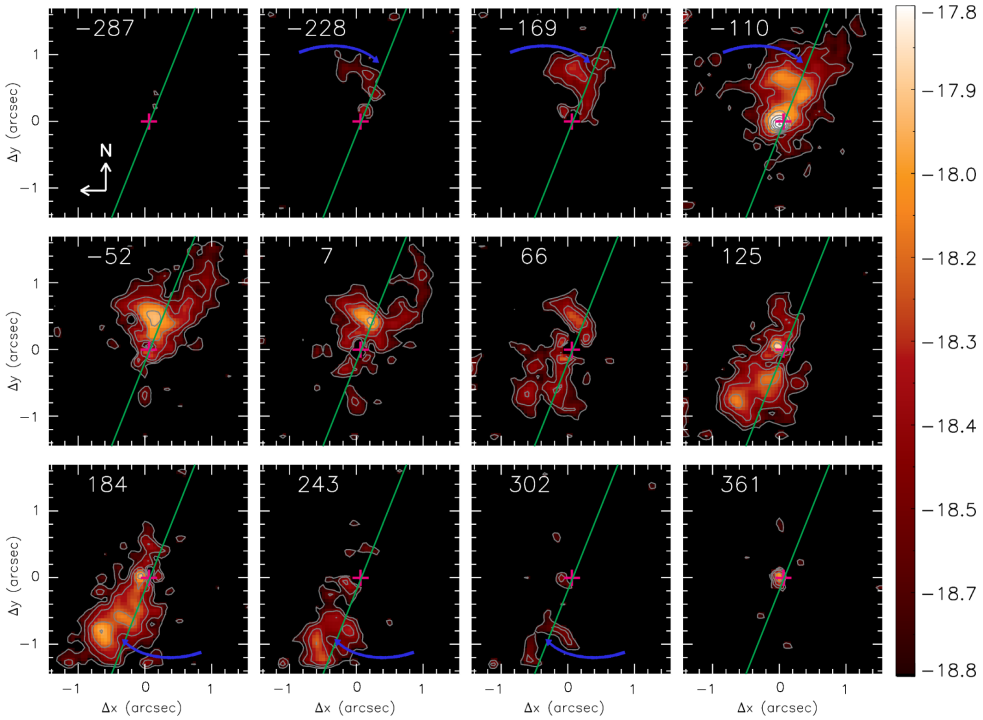

Figure 7. Same as Fig. 6 for Brγ.

with a mean fractional difference ($\sigma_{\rm frac} = (\sigma_{\rm CO} - \sigma_{\rm opt})/\sigma_{\rm opt}$) of 14.3 per cent, with some galaxies showing much higher discrepancies (as NGC 4569, with a fractional difference of 40 per cent). Integrating the *K*-band spectra over the whole FOV and using the PPXF code, as done in Section 3.1 we obtain $\sigma_* = 230 \pm 4$ km s^{-1}. Using the value of González Delgado et al. (2002), we find a fractional difference of −11 per cent, while using the value of Nelson & Whittle (1995) we obtain a difference of 4 per cent. These differences are of the order of the discrepancies found in Riffel et al. (2015a).

Using this result in the $M_\bullet$–$\sigma_\star$ relation (Graham et al. 2011), we obtain a mass for the SMBH of $M_\bullet = 2.7^{+3.5}_{-2.1} \times 10^8$ M$_\odot$, which agrees with value found by Moran et al. (2007) using a value for the velocity dispersion measured in optical observations. The $M_\bullet$ we have found in this work is also consistent with that of Durré & Mould (2014) obtained using the kinematics of the ionized gas (He I) to derive the mass enclosed in the inner 56 pc ($\approx 4 \times 10^8$ M$_\odot$).

4.2 Gas excitation

The H_2 molecule can be excited by processes such as heating of the gas by shocks (Hollenbach & McKee 1989) or by X-rays (Maloney, Hollenbach & Tielens 1996), known as thermal processes, and by non-thermal processes such as absorption of soft-UV (Black & van Dishoeck 1987) and far-UV at clouds with density larger than 10^4 cm^{-3} (Sternberg & Dalgarno 1989). The origin of the H_2 emission in AGN has been discussed in several recent studies, based on long-slit spectroscopy (Storchi-Bergmann et al. 1999; Reunanen, Kotilainen & Prieto 2002; Davies et al. 2005) and IFS (Riffel et al. 2006; Sánchez et al. 2009; Storchi-Bergmann et al. 2009; Mazzalay, Rodríguez-Ardila & Komossa 2010). In the *K* band there are several emission lines from H_2, which can be used to study their origin. We used the ratio H_2 λ2.2477/λ2.1218 to assess if the H_2 emission is due to a thermal or non-thermal process at locations A and B in Fig. 3. For thermal processes, typical values are ≈0.1–0.2, while for non-thermal processes, typical values are ≈0.55 (e.g. Mouri 1994; Reunanen et al 2002; Storchi-Bergmann et al. 2009). For NGC 2110, we find H_2 λ2.2477/λ2.1218 ≈ 0.15 for the position A and H_2 λ2.2477/λ2.1218 ≈ 0.11 for positions B and C, indicating that the H_2 is thermalized by shocks and/or by X-ray emission. However, the signal-to-noise ratio for the H_2 λ2.2477 emission line was not high enough to further investigate the H_2 λ2.2477/λ2.1218 ratio at other locations.

The lower vibrational energy states of the H_2 molecule can also be thermalized in high gas densities even if excited by far-UV radiation (Sternberg & Dalgarno 1989), and long-slit spectroscopy of the circumnuclear region of a few active galaxies suggests that the this might be the case of some objects (Davies et al. 2005).

Assuming that the H_2 is thermalized, we can find the excitation temperature by fitting the observed fluxes by the following equation (Scoville et al. 1982):

$$\log\left(\frac{F_i \lambda_i}{A_i g_i}\right) = \text{constant} - \frac{T_i}{T_{\rm exc}}, \qquad (2)$$

where F_i is the flux of the *i*th H_2 line, λ_i is its wavelength, A_i is the spontaneous emission coefficient, g_i is the statistical weight of the upper level of the transition, T_i is the energy of the level expressed as a temperature and $T_{\rm exc}$ is the excitation temperature. This equation assumes a ratio of transitions *ortho:para* of 3:1 and is valid only for thermal equilibrium, what seems to be the case for most AGN, as found in the studies discussed above: non-thermal processes contribute very little to the H_2 emission, at least in the cases that do not show intense star formation. In the case of NGC 2110, the H_2 λ2.2477/λ2.1218 ratio discussed above supports that the H_2 is thermalized.

In Fig. 9, we plot the $N_{\rm upp} = F_i\,\lambda_i/A_i\,g_i$ (plus an arbitrary constant) versus $E_{\rm upp} = T_i$ for the positions A, B and C shown in Fig. 3, in which ortho transitions are represented with open symbols and the

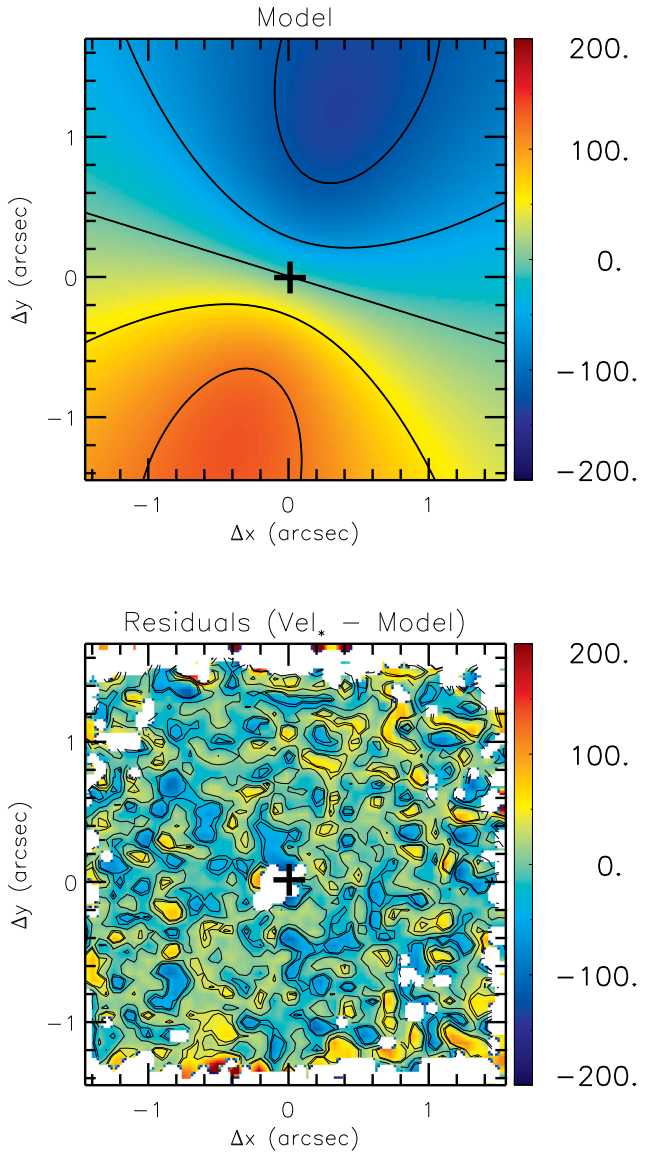

Figure 8. Rotating disc model for the stellar velocity field (top) and residual map between the observed and modelled velocities. The cross marks the position of the nucleus and the colour bar shows the range of velocities in km s^{-1}.

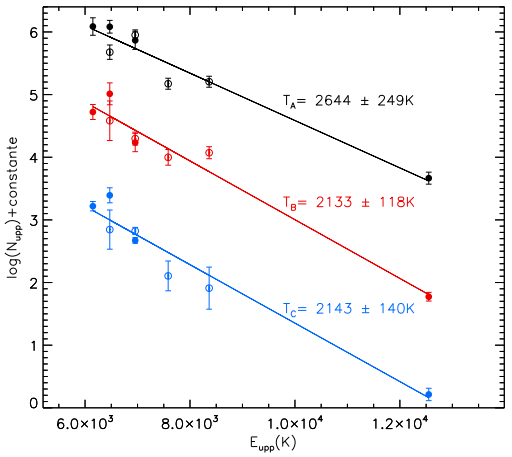

Figure 9. Relation between $N_{\rm upp} = F_i\,\lambda_i/A_i\,g_i$ and $E_{\rm upp} = T_i$ for the H_2 emission lines for thermal excitation at locations A, B and C (from top to bottom) in Fig. 3. *Ortho* transitions are shown as filled circles and *para* transitions as open circles.

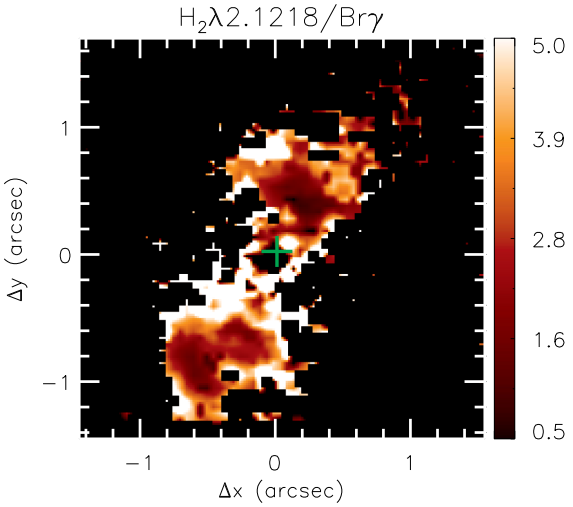

Figure 10. Line ratio map $H_2\,\lambda2.1218/{\rm Br}\gamma$.

best linear fit of equation (2) is shown as a continuous line. This result confirms the thermal excitation. Although the uncertainty in the fit might be high, since there is only one point at the high-energy region, it suggests that the vibrational and rotational states of the H_2 molecule are in thermal equilibrium and this favours thermal processes as the main excitation mechanism of the H_2 emission. The derived excitation temperatures for positions A, B and C are $T_{\rm A} = 2644 \pm 249$ K, $T_{\rm B} = 2133 \pm 118$ K and $T_{\rm C} = 2143 \pm 140$ K, respectively.

In order to further investigate the origin of the H_2 emission, we estimate the vibrational temperature ($T_{\rm vib}$) using the H_2 λ2.1218/2.2477 line ratio in $T_{\rm vib} = 5600/\ln(1.355 \times F_{\rm H_2\,\lambda2.1218}/F_{\rm H_2\,\lambda2.2477})$ (Reunanen et al. 2002) using the fluxes from Table 1. We find that $T_{\rm vib}$ is in the range 2260–2540 K, which are very similar to the values found above for the excitation temperature. The fact that the excitation temperature, obtained using both rotational and vibrational transitions, and the vibrational temperature are similar supports the assumption above that both rotational and vibrational states are thermalized.

We also investigated the excitation mechanism of the H_2 using the $H_2\,\lambda2.1218\,/{\rm Br}\gamma$ line ratio. In starbursts, where the main excitation mechanism is UV radiation, $H_2\,\lambda2.1218\,/{\rm Br}\gamma < 0.6$, while for AGN, where the H_2 is excited by shocks, by X-rays from the nucleus or by UV radiation, $0.6 < H_2\,\lambda2.1218\,/{\rm Br}\gamma < 2$, as found from long-slit spectroscopy for the nuclear aperture (Rodríguez-Ardila et al. 2004; Rodríguez-Ardila, Riffel & Pastoriza 2005). Recent studies using long-slit spectroscopy and IFU spectroscopy indicate a broader range of $H_2/{\rm Br}\gamma$ ratio values for AGN, with values in the range 0.6–6 (Riffel et al. 2013a) and 0.5–8 (Colina et al. 2015). Fig. 10 shows the $H_2/{\rm Br}\gamma$ line ratio map for NGC 2110, where the values are between 0.5 and 8 at most locations indicating excitation by the AGN. Approximately in 80 per cent of the points the values are larger than 2, but 91 per cent of the points show values between 0.5 and 8, thus still typical of Seyfert galaxies.

Our Brγ flux map (Fig. 3) presents a fairly similar structure to that seen in the [N II] flux map from Schnorr-Müller et al. (2014) and to

that found for the [O III] emission by Ferruit et al. (2004), where the ionized gas emission is stronger to the north of the nucleus than to the south, although the Brγ emission is less extended than both [N II] and [O III]. The Brγ emission is collimated along the direction south-east–north-west (PA $\approx -30^\circ/150^\circ$) that is the same orientation of the strongest gas emission in the optical as shown in Schnorr-Müller et al. (2014). The Brγ emission can thus be attributed to ionization by the collimated AGN radiation, which illuminates the galaxy disc in that direction. While in Schnorr-Müller et al. (2014) they have detected (much fainter) gas emission beyond this region of strongest emission, we are not able to detect this emission in Brγ, as this line is much less intense than the optical lines.

4.3 Mass of the molecular and ionized gas

The mass of hot H_2 in the inner 3 arcsec $\times$ 3 arcsec can be estimated as follows (Scoville et al. 1982):

$$M_{H_2} = \frac{2\, m_p\, F_{H_2\,\lambda2.1218}\, 4\pi\, d^2}{f_{v=1,J=3}\, A_{S(1)} h\, \nu} \approx 5.0776 \times 10^{13} \left(\frac{F_{H_2\,\lambda2.1218}}{\mathrm{erg\,s^{-1}\,cm^{-2}}}\right) \left(\frac{d}{\mathrm{Mpc}}\right)^2 [\mathrm{M_\odot}], \quad (3)$$

where m_p is the proton mass, $F_{H_2\,\lambda2.1218}$ is the flux of H_2 λ2.1218 μm emission line, d is the galaxy distance, h is the Planck constant and ν is the frequency of the H_2 line. We have assumed a typical vibrational temperature of $T_{vib} = 2000$ K (Storchi-Bergmann et al. 2009), which implies a population fraction $f_{v=1,J=3} = 1.22 \times 10^{-2}$ and a transition probability $A_{S(1)} = 3.47 \times 10^{-7}$ s^{-1} (Turner, Kirby-Docken & Dalgarmo 1977; Riffel et al. 2008). Integrating over the whole field of NIFS, the flux is $F_{H_2\,\lambda2.1218} \approx 3.1 \times 10^{-14}$ erg s^{-1} cm^{-2}, resulting in a hot molecular hydrogen mass of $M_{H_2} \approx 1.4 \times 10^3$ M$_\odot$. This value is in good agreement with those found for other AGN (Storchi-Bergmann et al. 2009; Riffel, Storchi-Bergmann & Nagar 2010; Riffel et al. 2013b). The amount of cold molecular gas may be much higher than the value derived above. Dale et al. (2005) found a ratio between the mass cold (M_{cold}) and hot molecular in the range 10^5–10^7 for a sample of six nearby galaxies, while Sánchez et al. (2009) found a ratio 1×10^6 for NGC 1068 and Mazzalay et al. (2013) obtained M_{cold}/M_{H_2} ranging from 10^5 to 10^8. We use here the conversion factor obtained by the most recent study of Mazzalay et al. (2013) because it includes more galaxies than the previous studies, which can be obtained from the expression:

$$\frac{M_{cold}}{\mathrm{M_\odot}} \approx 1174 \times \left(\frac{L_{H_2\,\lambda2.1218}}{\mathrm{L_\odot}}\right), \quad (4)$$

where $L_{H_2\,\lambda2.1218}$ is the luminosity of the H_2 line. We find $M_{cold} \approx 9.92 \times 10^8$ M$_\odot$, that is about six orders of magnitude larger than the mass of hot molecular gas.

The mass of ionized gas can be estimated from the measured flux of the Brγ emission line using the following expression (derived from the equations in Osterbrock & Ferland 2006):

$$M_{H\,II} \approx 3 \times 10^{17} \left(\frac{F_{Br\gamma}}{\mathrm{erg\,s^{-1}\,cm^{-2}}}\right) \left(\frac{d}{\mathrm{Mpc}}\right)^2 [\mathrm{M_\odot}], \quad (5)$$

where $F_{Br\gamma}$ is the integrated flux for the Brγ emission line and d (30.2 Mpc) is the distance to the galaxy. We assume an electron temperature $T = 10^4$ K and electron density $N_e = 500$ cm^{-3}. Integrating over the whole IFU field, we obtain $F_{Br\gamma} = 6.5 \times 10^{-15}$ erg cm^{-2} s^{-1}, resulting in $M_{H\,II} \approx 1.77 \times 10^6$ M$_\odot$.

Durré & Mould (2014), through adaptive optics near-IR IFS with the Keck OSIRIS instrument, found a total mass of ionized gas of 7.5×10^5 M$_\odot$ within an FOV of $\approx$2.3 $\times$ 1.8 arcsec. This value is about 40 per cent of the value we have obtained, but this is consistent with the fact that the area covered by our FOV is 2.2 times larger.

The mass of ionized gas derived for NGC 2110 is thus three orders of magnitude smaller than the estimated total mass of molecular gas, a result that is in agreement with those of previous studies (Ferruit et al. 2004; Riffel et al. 2008, 2013b; Storchi-Bergmann et al. 2009, 2010).

4.4 Kinematics of the emitting gas

The velocity fields of the H_2 and Brγ emitting gases (Fig. 4) are similar to the stellar one (Fig. 2), with blueshifts to the north-west and redshifts to the south-east of the nucleus. However, the H_2 kinematics shows deviations from rotation in regions next to the nucleus as well as in regions $\approx$1.0 arcsec to the north and south, which show a spiral pattern.

Although the inclination of the disc and orientation of the line of nodes obtained from the fit of the stellar velocity field are not that different from those obtained by Schnorr-Müller et al. (2014) for the gas in the optical, there are significant differences between the H_2 velocity field and the stellar velocity field. Several works indeed show that the gas and stellar kinematics are not always consistent with each other in the central region of galaxies (Stoklasová et al. 2009; Westoby et al. 2012; Davies et al. 2014; Riffel, Storchi-Bergmann & Riffel 2015b).

In order to isolate the non-circular components of the molecular gas velocity field, we fitted the H_2 velocity field using the equation (1), but keeping fixed the geometric parameters of the disc and the systemic velocity derived from the fitting of the stellar velocity field. This procedure allows us to derive the maximal rotation, which is expected to be larger for the gas than for the stars, since the gas may is usually located in a thin disc (while the stars have a higher velocity dispersion). The resulting best model is very similar to that for the stars (Fig. 8), but with a velocity amplitude of $A = 473 \pm 20$ km s^{-1}. We have built a residual map between the H_2 velocity field (Fig. 4) and the best-fitting disc model. This H_2 residual map is shown in Fig. 11. Assuming that the spiral arms are trailing, we conclude that the far side of the galaxy is the north-east and the near side is the south-west.

Beyond the inner 0.5 arcsec (73 pc) of the H_2 residual map, we find what seems to be a spiral arm in blueshift to the north and north-east of the nucleus in the far side of the galaxy, which could be due to gas flowing in towards the nucleus. In the near side of the galaxy, we find mostly redshifts, which can also be interpreted as due to inflows.

We thus interpret most of the residuals observed in Fig. 11 as being originated from gas in the plane of the galaxy flowing towards the nucleus. This interpretation is supported by the channel maps in H_2 shown in Fig. 6: in the channel maps from -245 down to -65 km s^{-1}, the blueshifted arm can be observed in the far side of the galaxy plane, while in the channel maps from 116 to 356 km s^{-1}, the redshifted arm can be observed in the near side of the galaxy plane, supporting inflows towards the line of nodes where a structure resembling a nuclear bar is observed in the lower velocity channels (blueshifts and redshifts). This bar runs from the north-west to the south-east, and is actually a bit tilted relative to the line of nodes.

Within the inner 0.5 arcsec (73 pc), the residual map of Fig. 11 shows blueshifts in the near side of the galaxy plane and redshifts in the far side along PA $\approx 90^\circ$ that we attribute to an H_2 nuclear outflow.

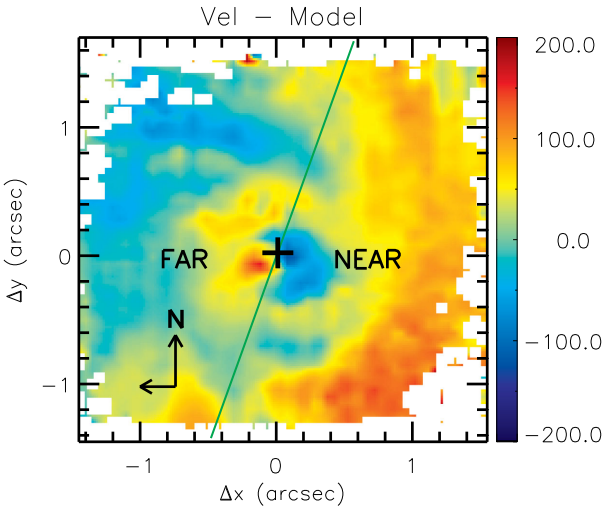

Figure 11. Velocity residual map for H_2 λ2.1218 μm obtained from the difference between the H_2 velocity field (Fig. 4) and the gas velocity model. The map is in units of km s^{-1}.

A compact outflow, but for the ionized gas, has been reported in previous optical long-slit observations by González Delgado et al. (2002), Rosario et al. (2010), as well as by our group in Schnorr-Müller et al. (2014) using optical IFS.

Schnorr-Müller et al. (2014) has found two kinematic components in disc rotation in NGC 2110, which they have called the 'warm' (higher velocity dispersion) and 'cold' (lower velocity dispersion) discs (their figs 11 and 12). Their velocity residual map for the warm component shows positive values to the north-east of the nucleus and negative values to the south-west of it, in a very compact structure (within the inner arcsec). They interpreted this component as a nuclear outflow, and we conclude it could be identified with the compact outflow we see in H_2 (Fig. 11). Similarly, the velocity residual map for the cold component of Schnorr-Müller et al. (2014) shows some excess redshifts to the south-west and blueshifts to the north-east that are similar to the residuals found in the H_2 kinematics, which we thus identify with the inflows we have found in H_2.

4.4.1 *Feeding of the AGN*

Once we have concluded that the molecular gas kinematics suggest the presence of inflows towards the centre, we can use the velocity field maps to estimate the mass inflow rate as follows:

$$\dot{M}_{H_2} = 2\, m_p\, N_{H_2}\, v\, \pi\, r^2\, n_{arms}, \quad (6)$$

where m_p is the proton mass, $v = v_{obs}/\sin i$ is the velocity of the gas flowing towards the centre in the plane of the galaxy, $v_{obs} = 80$ km s^{-1} is the observed velocity in H_2 the residual map and $i = 42°$ is the disc inclination relative to the plane of the sky (González Delgado et al. 2002). This value of i is very similar to that obtained by fitting the stellar kinematics ($i \approx 43°$). We adopt $r = 0.3$ arcsec (≈ 44 pc) as the radius of a circular cross-section in the nuclear arm to the north/north-east of the nucleus at 1 arcsec from the nucleus. N_{H_2} is the molecular gas density and $n_{arms} = 2$ is the number of spiral arms. We have assumed that the molecular gas is located in a disc with radius $r_d = 1.5$ arcsec (220 pc) corresponding to the NIFS FOV and a typical thickness of $h = 30$ pc (Hicks et al. 2009).

The value of the gas density was obtained from

$$N_{H_2} = \frac{M_{H_2}}{2\, m_p\, \pi\, r_d^2\, h}. \quad (7)$$

We find $N_{H_2} \approx 6.22 \times 10^{-3}$ cm^{-3}, which results in an inflow rate of $\approx 4.55 \times 10^{-4}$ $M_\odot$ yr^{-1}. The inflow rate derived above is small, and might be only a fraction of the total molecular gas flowing towards the centre of the galaxy, as the warm molecular gas we observe in the near-IR may only be the heated skin of a much larger reservoir of cold molecular gas, as we have discussed in Section 4.3. Using the conversion factor for the cold/warm molecular gas obtained in Section 4.3, we find that the molecular gas mass inflow rate could be higher than 10 $M_\odot$ yr^{-1},

4.4.2 *Feedback of the AGN*

As we have also found outflows within the inner 0.5 arcsec (73 pc), we can also calculate their power. These outflows have been identified as the blueshifts and redshifts in the residual velocity map of the molecular hydrogen (Fig. 11) along PA ≈120° within the inner 0.5 arcsec.

The outflow observed in H_2 has a similar orientation to that of the compact outflow seen in ionized gas by Schnorr-Müller et al. (2014), who also concluded that the outflow is not oriented along the ionization cone. Outflows not co-spatial with the ionization cone have been observed for other active galaxies.

Riffel et al. (2014) report an equatorial outflow detected using NIFS observations for the Seyfert 2 NGC 5929 (see also Riffel et al. 2015b). For NGC 2110 we proposed that the outflow is a result from gas in the plane of the galaxy being pushed by clouds outflowing from the nucleus. The same hypothesis was put forth by Schnorr-Müller et al. (2014), where the authors observed a compact outflow from the nucleus of NGC 2110, suggesting a spherical geometry, using optical IFS. In the case of H_2, most of the gas is concentrated at the disc of the galaxy, and thus the interaction of the expanding spherical bubble is seen only at locations where the H_2 is present, forming the bipolar structure seen in the residual map.

On the basis of our and other's previous studies of the morphology of the outflow (as its extent is of the order of the point spread function FWHM), we assume a biconical structure with an opening angle of 60° with a radius $r \approx 31$ pc (consistent with the constraints posed by the flux distribution of the outflowing gas) and use the following expression:

$$\dot{M}_{out} = \frac{2\, m_p\, N_{H_2}\, v\, \pi\, r^2\, n}{\mathrm{sen}\,\theta}, \quad (8)$$

where v is the outflowing gas velocity, $n = 2$ accounts for the two sides of the bicone and θ is the angle that the central axis of the cone makes with the plane of the sky. The velocity can be obtained directly from Fig. 11 and is $v = 70$ km s^{-1}. Using the estimated $\theta = 18°$ by Rosario et al. (2010), we obtain $\dot{M}_{out} = 4.3 \times 10^{-4}$ $M_\odot$ yr^{-1}. But again, as for the mass inflow rate, the total mass outflow rate, that is probably dominated by the cold molecular gas, can be five to seven orders of magnitudes higher. The mass outflow rate obtained for the ionized gas by Schnorr-Müller et al. (2014) is 0.9 $M_\odot$ yr^{-1}, thus much higher than that in the warm molecular gas, although it may be comparable to that in

the cold molecular gas in NGC 2110, as discussed above. This result for NGC 2110 differs from those we have obtained for most galaxies we have studied so far, where the H_2 gas is usually rotating in the galaxy plane or in inflow. It is seldom found in outflow. Outflows are more frequently found in the ionized gas (e.g. Storchi-Bergmann et al. 2010; Riffel & Storchi-Bergmann 2011a; Riffel et al. 2013b; Schnorr-Müller et al. 2014).

Durré & Mould (2014) report the presence of a nuclear bar seen in the [Fe II] flux map, but the velocity field observed in [Fe II] shows only blueshifts, although this depends on the adopted systemic velocity. The PA of this bar, as well as its extent (≈90 pc), is consistent with what we have interpreted as an outflow seen in our H_2 velocity map, which shows blueshifts to one side of the nucleus but redshifts to the other side. If this structure is a bar, one possibility is that the inflows are feeding the bar, whose orientation (PA $\sim 125^\circ$) is close to the galaxy major axis (PA $\sim 162^\circ$). Unfortunately, we do not have observations in the *J* or *H* band to compare the [Fe II] emitting gas kinematics with that of the H_2 emitting gas. Further observations and modelling would be necessary in order to settle on the nature of this feature.

4.4.3 AGN accretion rate

The inflow and outflow rates estimated above can be compared to the accretion rate on to the SMBH that is needed to power the AGN. The mass accretion rate to the AGN can be estimated via

$$\dot{m} = \frac{L_{\rm bol}}{c^2 \eta}, \tag{9}$$

where c is the speed of light, η is the efficiency of conversion of matter into energy (for Seyfert galaxies $\eta \approx 0.1$) and $L_{\rm bol}$ is the AGN bolometric luminosity. The X-ray luminosity of the AGN in NGC 2110 is estimated as $L_{\rm X} = 2.9 \times 10^{42}$ erg s^{-1} (Pellegrini 2010), and in order to obtain the bolometric luminosity we adopt the usual relation $L_{\rm bol} = 10\,L_{\rm X}$. The resulting accretion rate is thus $\dot{m} = 1.6 \times 10^{-3}$ M$_\odot$ yr^{-1}.

If we use instead the bolometric luminosity from Rosario et al. (2010), of $L_{\rm bol} = 5 \times 10^{43}$ erg s^{-1}, we obtain a somewhat larger value of $\dot{m} = 2.8 \times 10^{-3}$ M$_\odot$ yr^{-1} than that obtained above.

The accretion rate is approximately one order of magnitude higher than the inflow and outflow rates in warm molecular gas, indicating that more mass flows towards the centre to feed the SMBH, but, as pointed above, the inflowing mass is probably dominated by cold molecular gas.

The mass inflow rate in warm H_2 obtained for NGC 2110 is similar to those obtained for other Seyfert galaxies (Riffel et al. 2009, 2010; Storchi-Bergmann et al. 2010) with similar luminosities to that of NGC 2110. The outflow rate in warm molecular gas is about three orders of magnitude smaller than mass outflow rates we have observed in ionized gas for other Seyfert galaxies (e.g. Riffel et al. 2008, 2013b; Sánchez et al. 2009) and up to six orders of magnitude smaller than those observed for high-luminosity Seyfert 2 galaxies (e.g. McElroy et al. 2014). But the compact outflow we have observed in warm H_2 for NGC 2110 may represent only a small fraction of the total outflow from the nucleus of this galaxy, which is probably also dominated by cold molecular gas. A possible scenario for the inner region of NGC 2110 is that the inflows observed in H_2 feed the central region of the galaxy and the accreted gas then triggers both star formation and the nuclear activity. Indeed, young stellar clusters have been observed around the nucleus of NGC 2110 by Durré & Mould (2014).

5 CONCLUSIONS

Using IFS in the near-IR obtained with the Gemini instrument NIFS, we have mapped the stellar and gaseous kinematics within the inner ≈250 pc of the Seyfert 2 galaxy NGC 2110, as well as the ionized and molecular gas flux distributions at an angular resolution 0.15 arcsec. Our main conclusions are as follows.

(i) The stellar kinematics shows velocity dispersion reaching ≈250 km s^{-1} around the nucleus as well as a rotation pattern with a similar velocity amplitude.

(ii) From the $M_\bullet$–$\sigma_\star$ relation, we estimate the mass of the SMBH as $M_\bullet = 2.7^{+3.5}_{-2.1} \times 10^8$ M$_\odot$.

(iii) The flux distributions of the H_2 and Brγ emission lines are different: while the Brγ flux seems to be collimated along PA ≈ −30° (from south-east to north-west), the H_2 emission is observed over the whole FOV.

(iv) From the emission-line ratios, we conclude that the H_2 emission is due to thermal processes (heating X-rays from the AGN and/or shocks), with an excitation temperature in the range ≈2100–2700 K.

(v) The warm molecular gas and ionized gas masses within the observed FOV were estimated as $M_{\rm H_2} \approx 1.4 \times 10^3$ M$_\odot$ and $M_{\rm H\,II} \approx 1.7 \times 10^6$ M$_\odot$, respectively;

(vi) The velocity field of the gas shows a rotation pattern similar to that observed for the stars. However, deviations from this pattern are observed, due to both inflows and outflows, more clearly in the molecular gas emission, as the ionized gas emission covers just a small part of the FOV.

(vii) Inflows in warm H_2 along spiral arms are observed beyond the inner ≈70 pc, at a mass inflow rate of 4.6×10^{-4} M$_\odot$ yr^{-1}.

(viii) Outflows in warm H_2 are observed within the inner ≈70 pc, at a mass outflow rate of 4.3×10^{-4} M$_\odot$ yr^{-1}.

The uncertainties in the above mass flow rates might be high due to assumptions about the gas density and geometry. They are one order of magnitude lower than the accretion rate to the AGN. But we point out that these rates are in warm molecular gas, which may be only the heated skin of a much larger cold molecular gas reservoir. If we consider that previous observations of both warm and cold molecular gas in nearby AGNs reveal that typical ratios between the cold and warm molecular gas masses are in the range 10^5–10^7, the above flow rates may be as high as a few to tens of solar masses per year. Similarly, the total mass of molecular gas may reach 10^9 M$_\odot$.

ACKNOWLEDGEMENTS

We acknowledge the referee for valuable suggestions that helped to improve the paper. This work is based on observations obtained at the Gemini Observatory, which is operated by the Association of Universities for Research in Astronomy, Inc., under a cooperative agreement with the NSF on behalf of the Gemini partnership: the National Science Foundation (United States), the Science and Technology Facilities Council (United Kingdom), the National Research Council (Canada), CONICYT (Chile), the Australian Research Council (Australia), Ministério da Ciência e Tecnologia (Brazil) and South-EastCYT (Argentina). This research has made use of the NASA/IPAC Extragalactic Database (NED) which is operated by the Jet Propulsion Laboratory, California Institute of Technology, under contract with the National Aeronautics and Space Administration. This work has been partially supported by the Brazilian institution CNPq. RAR acknowledges support from FAPERGS (project No. 12/1209-6) and CNPq (project No. 470090/2013-8).

REFERENCES

Aalto S., Garcia-Burillo S., Muller S., Winters J. M., van der Werf P., Henkel C., Costagliola F., Neri R., 2012, A&A, 573, 44
Barbosa F. K. B., Storchi-Bergmann T., Vale T. B., McGregor P., 2014, MNRAS, 445, 2353
Bertola F., Bettoni D., Danziger J., Sadler E., Sparke L., de Zeeuw T., 1991, ApJ, 373, 369
Black J. H., van Dishoeck E. F., 1987, ApJ, 322, 412
Bradt H. V., Burke B. F., Canizares C. R., Greenfield P. E., Kelley R. L., McClintock J. E., van Paradijs J., Koski A. T., 1978, ApJ, 226, 111
Cappellari M., Emsellem E., 2004, PASP, 116, 138
Colina L. et al., 2015, A&A, 578, A48
Dale D. A., Sheth K., Helou G., Regan M. W., Hüttemeister S., 2005, ApJ, 129, 2197
Davies R. I., Sternberg A., Lehnert M. D., Tacconi-Garman L. E., 2005, ApJ, 633, 105
Davies R. I., Maciejewski W., Hicks E. K. S., Tacconi L. J., Genzel R., Engel H., 2009, ApJ, 702, 114
Davies R. I. et al., 2014, ApJ, 792, 101
Durré M., Mould J., 2014, ApJ, 784, 79
Evans D. A., Lee J. C., Kamenetska M., Gallagher S. C., Kraft R. P., Hardcastle M. J., Weaver K. A., 2006, ApJ, 653, 1121
Ferrarese L., Ford H., 2005, Space Sci. Rev., 116, 523
Ferruit P., Mundell C. G., Nagar N. M., Emsellem E., Pécontal E., Wilson A. S., Schinnerer E., 2004, MNRAS, 352, 1180
González Delgado R. M., Heckman T., Leitherer C., 2001, ApJ, 546, 845
González Delgado R. M., Arribas S., Pérez E., Heckman T., 2002, ApJ, 579, 188
Graham A. W., Onken C. A., Athanassoula E., Combes F., 2011, MNRAS, 412, 2228
Heckman T., Best P., 2014, ARA&A, 52, 589
Hicks E. K. S., Davies R. I., Malkan M. A., Genzel R., Tacconi L. J., Sánchez F. M., Sternberg A., 2009, ApJ, 696, 448
Hicks E. K. S., Davies R. I., Maciejewski W., Emsellem E., Malkan M. A., Dumas G., Müller-Sánchez F., Rivers A., 2013, ApJ, 768, 107
Hollenbach D., McKee C. F., 1989, ApJ, 342, 306
Kormendy J., Ho L. C., 2013, ARA&A, 51, 511
McElroy R., Croom S. M., Pracy M., Sharp R., Ho I. -T., Medling A. M., 2014, MNRAS, 446, 2186
McGregor P. J. et al., 2003, Proc. SPIE, 4841, 1581
Malkan M. A., Gorjian V., Tam R., 1998, ApJS, 117, 25
Maloney P. R., Hollenbach D. J., Tielens A. G. G. M., 1996, ApJ, 466, 561
Markwardt C. B., 2009, in Bohlender D. A., Durand D., Dowler P., eds, ASP Conf. Ser. Vol. 411, Astronomical Data Analysis Software and Systems XVIII. Astron. Soc. Pac., San Francisco, p. 251
Martini P., Dicken D., Storchi-Bergmann T., 2013, ApJ, 766, 121
Mazzalay X., Rodríguez-Ardila A., Komossa S., 2010, MNRAS, 405, 1315
Mazzalay X. et al., 2013, MNRAS, 428, 2389
Mazzalay X. et al., 2014, MNRAS, 438, 2036
Moran E. C., Barth A. J., Eracleous M., Kay L. E., 2007, ApJ, 668, L31
Mouri H., 1994, ApJ, 427, 777
Nagar N. M., Wilson A. S., Mulchaey J. S., Gallimore J. F., 1999, ApJS, 120, 209
Nelson C. H., Whittle M., 1995, ApJS, 99, 67
Osterbrock D. E., Ferland G. J., 2006, Astrophysics of Gaseous Nebulae and Active Galactic Nuclei, 2nd edn. University Science Books, Mill Valley, CA
Pellegrini S., 2010, ApJ, 717, 640
Plummer H. C., 1911, ApJ, 71, 460
Quillen A. C., Alonso-Herrero A., Rieke M. J., McDonald C., Falcke H., Rieke G. H., 1999, ApJ, 525, 685
Reunanen J., Kotilainen J. K., Prieto M. A., 2002, MNRAS, 331, 154
Riffel R. A., 2010, Ap&SS, 327, 239
Riffel R. A., Storchi-Bergmann T., 2011a, MNRAS, 411, 469
Riffel R. A., Storchi-Bergmann T., 2011b, MNRAS, 417, 2752
Riffel R. A., Sorchi-Bergmann T., Winge C., Barbosa F. K. B., 2006, MNRAS, 373, 2
Riffel R. A., Storchi-Bergmann T., Winge C., McGregor P. J., Beck T., Schmitt H., 2008, MNRAS, 385, 1129
Riffel R. A., Storchi-Bergmann T., Dors O. L., Winge C., 2009, MNRAS, 393, 783
Riffel R. A., Storchi-Bergmann T., Nagar N. M., 2010, MNRAS, 404, 166
Riffel R., Rodriguez-Ardila A., Aleman I., Brotherton M. S., Pastoriza M. G., Bonatto C., Dors O. L., 2013a, MNRAS, 430, 2002
Riffel R. A., Storchi-Bergmann T., Winge C., 2013b, MNRAS, 430, 2249
Riffel R. A. et al., 2015a, MNRAS, 446, 2823
Riffel R. A., Storchi-Bergmann T., Riffel R., 2014, ApJ, 780, L24
Riffel R. A., Storchi-Bergmann T., Riffel R., 2015b, MNRAS, 451, 3587
Rodríguez-Ardila A., Pastoriza M. G., Viegas S., Sigut T. A. A., Pradhan A. K., 2004, A&A, 425, 457
Rodríguez-Ardila A., Riffel R., Pastoriza M. G., 2005, MNRAS, 364, 1041
Rosario D. J., Whittle M., Nelson C. H., Wilson A. S., 2010, MNRAS, 408, 565
Sakamoto K., Aalto S., Evans A. S., Wiedner M. C., Wilner D. J., 2010, ApJ, 725, L228
Sánchez F. M., Davies R. I., Genzel R., Tacconi L. J., Eisenhauer F., Hicks E. K. S., Friedrich S., Sternberg A., 2009, ApJ, 691, 749
Schnorr-Müller A., Storchi-Bergmann T., Nagar N. M., Robinson A., Lena D., Riffel R. A., Couto G. S., 2014, MNRAS, 437, 1708
Schönell A. J., Jr, Riffel R. A., Storchi-Bergmann T., Winge C., 2014, MNRAS, 445, 414
Scoville N. Z., Hall D. N. B., Ridgway S. T., Keinmann S. G., 1982, ApJ, 253, 136
Simões Lopes R. D., Storchi-Bergmann T., de Fátima Saraiva M., Martini P., 2007, ApJ, 655, 718
Somerville R. S., Hopkins P. F., Cox T. J., Robertson B. E., Hernquist L., 2008, MNRAS, 391, 481
Sternberg A., Dalgarno A., 1989, ApJ, 338, 197
Stoklasová I., Ferruit P., Emsellem E., Jungwiert B., Pécontal E., Sánchez S. F., 2009, A&A, 500, 1287
Storchi-Bergmann T., Winge C., Ward M., Wilson A. S., 1999, MNRAS, 304, 35
Storchi-Bergmann T., McGregor P., Riffel R. A., Simões Lopes R., Beck T., Dopita M., 2009, MNRAS, 394, 1148
Storchi-Bergmann T., Simões Lopes R., McGregor P., Riffel R. A., Beck T., Martini P., 2010, MNRAS, 402, 819
Turner J., Kirby-Docken K., Dalgarmo A., 1977, ApJ, 35, 281
Ulvestad J. S., Wilson A. S., 1983, ApJ, 264, L7
Veilleux S. et al., 2013, ApJ, 776, 27
Weaver K. A., Mushotzky R. F., Serlemitsos P. J., Wilson A. S., Elvis M., Briel U., 1995, ApJ, 442, 597
Westoby P. B., Mundell C. G., Nagar N. M., Maciejewski W., Emsellem E., Roth M. M., Gerssen J., Baldry I. K., 2012, ApJS, 199, 1
Wilson A. S., Baldwin J. A., 1985, ApJ, 289, 124
Wilson A. S., Baldwin J. A., Ulvestad J. S., 1985, ApJ, 291, 627
Winge C., Riffel R. A., Storchi-Bergmann T., 2009, ApJS, 185, 186

This paper has been typeset from a TEX/LATEX file prepared by the author.